Supporting Information

pH-independent lead sequestration and light management enable sustainable and efficient perovskite photovoltaics

Xi Jin, ‡ [abc] Jun Li, ‡[a] Siyuan Zhu, [cd] Wenyan Tan, [bc] Jiahong Tang, [a] Xueyuan Gong, [e] Xingyu Liu, [a] Yu Zhang, [bc] Chao Zhou, [c] Zhaoheng Tang, [c] Vincent O. Nyamori, [f] Bice S. Martincigh, [f] Matthew L. Davies, [fg] Minghua Li, [eh] Tongsheng Chen, [b] Qi Chen, [a] Jinsong Hu, [e] Qijie Liang, *[c] Weiqiang Chen *[b] and Yan Jiang *[a]

a X. Jin, J. Li, J. Tang, X. Liu, Q. Chen, Y. Jiang
School of Materials Science and Engineering
Beijing Institute of Technology
Beijing 100081(China)
E-mail: yan.jiang@bit.edu.cn

b X. Jin, W. Tan, Y. Zhang, T. Chen, W. Chen
MOE Key Laboratory of Laser Life Science & Guangdong Provincial Key Laboratory of Laser Life Science, Guangzhou Key Laboratory of Spectral Analysis and Functional Probes, College of Biophotonics
South China Normal University
Guangzhou 510631 (China)
E-mail: achenweiqiang@m.scnu.edu.cn

c X. Jin, S. Zhu, W. Tan, Y. Zhang, C. Zhou, Z. Tang, Q. Liang
Songshan Lake Materials Laboratory
Beijing Institute of Technology
Dongguan 523429 (China)
E-mail: liangqijie@sslab.org.cn

d S. Zhu
Department of Physics
Liaoning University
Shenyang 110036 (China)

e X. Gong, M. Li, J. Hu
Beijing National Laboratory for Molecular Sciences (BNLMS), Institute of Chemistry
Chinese Academy of Sciences,
Beijing 100190 (China)

f V. Nyamori, B. Martincigh, M. Davies
School of Chemistry and Physics
University of KwaZulu-Natal
Private Bag X54001, Durban, 4000 (South Africa)

g M. Davies
SPECIFIC IKC, Materials Science and Engineering, Faculty of Science and Engineering
Swansea University
Singleton Park, Swansea, Wales SA2 8PP (UK)

h M. Li
College of Chemical Engineering Beijing Advanced Innovation Center for Soft Matter Science and Engineering
Beijing University of Chemical Technology
Beijing 100029 (China)

* Corresponding author

This file includes:

1. Experimental section

Materials

Pre-patterned ITO glass substrates were purchased from Advanced Election Technology CO. Ltd. N, N-dimethylformamide (DMF), dimethyl sulfoxide (DMSO), isopropanol (IPA), acetonitrile (ACN), chlorobenzene (CB), 4-tert-butylpyridine (tBP), cesium iodide (CsI), potassium iodide (KI), bis(trifluoromethane)sulfonimide lithium salt (Li-TFSI) and MoO_X were purchased from Sigma-Aldrich. Formamidinium iodide (FAI), methylammonium chloride (MACl), and methylammonium bromide (MABr) were purchased from Greatcell Solar. Lead iodode (PbI_2) was purchased from TCI. Spiro-MeOTAD, 2-phenylethylamine hydroiodide (PEAI) were purchased from Xi'an Polymer Light Technology. Tin (IV) oxide (SnO_2) colloidal solution (15% in H_2O) was purchased from Alfa Aesar. Poly (vinyl alcohol) (PVA) (degree of alcoholysis: 98.0–99.0 mol%, viscosity: 54.0-66.0 mPa.s), Concentrated Phosphoric acid (H_3PO_4) (≥85 wt.% in H_2O), Urea, Potassium phosphate dibasic anhydrous (K_2HPO_4), and Glycerol ($C_3H_8O_3$) were purchased from Aladdin. Besides, High-purity Ag electrode material was purchased from commercial sources.

Precursor Preparation.

The precursor of SnO_2 electron transporting layer was prepared by mixing SnO_2 colloidal solution with deionized water by a volume ratio of 1:3. The PbI_2 solution was obtained by dissolving 0.13 M CsI, 0.025 M KI and 1.3 M PbI_2 in mixed anhydrous solvent (DMF:DMSO is 19:1). The FAI solution was prepared by dissolving 60 mg of FAI, 6 mg of MABr and 6 mg of MACl in 1 ml IPA. The PEAI solution (20 mM) was obtained by dissolving 5 mg PEAI powder in 1 mL IPA. 72.3 mg of Spiro-MeOTAD, 28.5 μL of tBP and 17.5 μL of Li-TFSI (520 mg/mL in acetonitrile) were mixed in 1 mL CB to prepare the Spiro-OMeTAD solution. All of the above solutions were filtered by 0.22 μm filters before use. 2PACz solution was prepared by dissolving 1.5 mg 2PACz in 5 mL of ethanol solution. $(Cs_{0.15}FA_{0.85})Pb(I_{0.95}Br_{0.05})_3$ was obtained by dissolving 0.6579 g of FAI, 0.1437 g of CsBr and 2.0745 g of PbI_2 in 3 mL of an organic mixture (DMF: DMSO = 4:1, v/v).

Device Fabrication.

The PSCs fabrication: Pre-patterned ITO glass substrates were cleaned with anhydrous alcohol and acetone using an ultrasonic cleaner. Then, the substrates were dealt with ultraviolet ozone for 30 min. To prepare SnO_2 thin film, 100 μL SnO_2 nanocrystal colloidal solution was spin-coated onto the cleaned ITO substrate at 4000 rpm for 30 s, followed by drying at 150 °C for 30 min in ambient air. The films were cooled down and dealt with ultraviolet ozone for 30 min. PbI_2 solution was spin-coated at a rate of 1500 rpm for 30s, followed by thermal annealing at 70 °C for 1 min in nitrogen. Then the FAI solution was spin-coated onto PbI_2 at a rate of 1500 rpm for 30s, followed by thermal annealing at 150 °C for 15 min in ambient air (30-50% humidity). After the as-prepared perovskite substrates cooled down, 50 μL PEAI solution was spin-coated onto perovskite films at 5000 rpm for 30 s in an N_2 glove box. Then 50 μL the spiro-OMeTAD solution solution was deposited on the as-prepared perovskite substrates with a rate of 3000 rpm for 30 s and the films were stored in a drying cabinet (25 ℃, RH 5-10%) overnight. Finally, 10 nm MoO_3 and 60 nm Ag were deposited by thermal evaporation under a high vacuum condition (<10^{-5} Pa). The illumination area of the device was 0.09 cm^2 controlled by a metal mask.

The F-PSCs fabrication: Pre-patterned ITO PEN substrates were cleaned with deionized water and anhydrous alcohol. Then, the substrates were dealt with ultraviolet ozone for 30 min. To prepare 2PACz thin film, 100 μL 2PACz solution was spin-coated onto the cleaned PEN substrate at 3000 rpm for 30 s, followed by drying at 100 °C for 5 min in ambient air. The films were cooled down and dealt with ultraviolet ozone for 30 min. Perovskite precursor solution was spin-coated at a rate of 6000 rpm for 30s, at the 15th second, 200 μL of CB was added dropwise and at the end of spin-coating, followed by thermal annealing at 150 °C for 20 min in nitrogen. Finally, 20 nm C_{60}, 8 nm BCP and 100 nm Ag were deposited by thermal evaporation under a high vacuum condition, respectively. The illumination area of the device was 0.09 cm^2 controlled by a metal mask.

PSMs fabrication: The structure of PSMs is consistent with rigid PSCs. The PSMs were fabricated on 5 cm × 5 cm substrates with six sub-cells connected in series. A P1 line (90 μm width) was laser scribed to isolated ITO substrates. A P2 line (105 μm width) was laser etched after deposition of the ETL, perovskite layer and HTL. Finally, a P3 line (100 μm width) was mechanically scribed after the deposition of an 80-nm-thick copper electrode.

Device encapsulation: The perovskite devices were encapsulated by a 1-mm-thick cover glass using ultraviolet-curable resin (UV resin).

PFPF Synthesis.

The H_3PO_4 solution was prepared by mixing concentrated H_3PO_4 solutions with deionized water by a volume ratio of 1:38. The K_2HPO_4 solution (0.344 M) was obtained by dissolving 60 mg K_2HPO_4 powder in 1 mL DI water. First, the PVA solution was obtained by adding 0.5 g PVA to 20 mL of deionized water, and magnetic stirred reaction for 2 h at 90 ℃ until completely dissolved. Then,

200 μL the H_3PO_4 solution was added to the PVA solution, stirred and heated for 1 h. To prepare PVA/PoB, 1mL K_2HPO_4 solution was added to the mixed solution of PVA and H_3PO_4, and kept stirring and heating for 1 h. The PFPF was obtained by adding 0.5 mL $C_3H_8O_3$ to the PVA/PoB solution and stirring for 1 h. The product was cooled down to room temperature and dried for 24-72 h until the film solidified. The PFPF was obtained by pouring the PFPF solution into a petri dish containing a silicon wafer. The product was cooled down to room temperature and dried for 24-72 h until the film solidified. After the PFPF is cured, it is removed from the wafer. The non-textured side of PFPF was attached to the substrate of rigid or flexible PSCs.

Characterization.

The *J-V* characteristics of photovoltaic devices were measured with a solar simulator (Newport) under AM 1.5 G standard irradiation (1000 W/m^2) in a nitrogen atmosphere (25 ℃), and Keithley 2400 source meter. Intensity of the solar simulator was calibrated using a certified monocrystalline silicon solar cell (KG5). The active areas of devices are 0.09 cm^2, which are defined by metal masks. XPS characterizations were performed by using Thermo Fisher ESCALAB Xi+ (Al Kα source), and core level C 1s (C-C bond of 284.8 eV) was used as the reference to calibrate the energy position. FTIR was operated by using Bruker INVENIO-R. XRD patterns were measured by using Bruker D8 Advance X-ray diffractometer (Cu Kα radiation). FE-SEM images were obtained by Zeiss Gemini SEM 300. The IPCE spectra were tested by QE-R3-011 measurement system from EnLi Technology. The Pb^{2+} concentrations were tested by using the Inductively coupled Plasma-Mass Spectrometry (Agilent 7800) and Inductively Coupled Plasma-Optical Emission Spectrometer (iCAP 7200).

Lead sequestration tests.

All glassware used in the lead adsorption test was thoroughly cleaned with detergent and DI water.

Pb(II) sequestration test: To simulate extreme rainfall conditions, each square centimeter of PSC is soaked in rainwater with a volume of over 9 mL.[1] After soaking the 1.5 × 1.5 cm^2 PSC in 20 mL of deionized (DI) water for 3 h, the Pb^{2+} concentration was below 20 mg/L. Therefore, 1.5 × 1.5 cm^2 PVA and PFPFs with different formulas were soaked in 20 mL of 20 mg/L Pb^{2+} solutions prepared by PbI_2 for 3 h. The Pb^{2+} concentrations were measured by ICP-MS and ICP-OES. The pH of the Pb^{2+} solutions was measured by a pH meter.

pH buffer performance test: To investigate the pH buffering capacity, we continuously added acidic water (pH = 4.2) to 10 ml of DI water with and without 1.5 × 1.5 cm^2 PFPF and recorded the pH evolution.

Pb(II) sorption kinetics test: 2.5 × 2.5 cm^2 PFPF (~69.1 mg) was added to a beaker containing 56 mL of 20 mg/L PbI_2 solution and stirred at room temperature. 0.5 mL of the supernatant was removed at different times (0.05, 0.1, 0.167, 0.5, 3, 5, 10, 30, 60,90 and 180 min). All supernatants were diluted with DI water and filtered through a 0.22 μm membrane filter. The remaining Pb(II) content was quantified by ICP-OES and ICP-MS.

Pb(II) sorption isotherm test: Lead (II) nitrate solutions of different concentrations (10, 30, 60, 120, 300 and 600 mg L^{-1}) were prepared with DI water 1.5 × 1.5 cm^2 PFPF (~23.9 mg) was added to a volumetric flask containing 5 mL of lead(II) solution of different concentrations. The mixture was stirred at room temperature for 3 hours. 1 mL of the supernatant was obtained, diluted with deionized water, filtered through a 0.22 μm membrane, and analyzed by ICP-OES.

Lead leakage tests.

All glassware used in the lead leakage test was cleaned with detergent and deionized water. The encapsulated PSCs and modules were damaged using a metal ball (45 mm diameter, 360 g) dropped from a height of 5 cm to simulate a heavy hailstorm.[2]

Soak test: Each damaged cell was placed in a 100 mL beaker containing 36 ml of DI water (For testing of lead leakage of PSM, each damaged PSM was placed in a 500 mL beaker containing 225 mL of simulated acid rain.) to ensure that the entire cell was completely submerged. The solution was stirred at room temperature for 3 hours to accelerate the leakage of lead from damaged devices. 0.5 mL of the supernatant was removed at different times (0.5, 1, 1.5, 2, 2.5 and 3 h). All supernatants were diluted with DI water and filtered through a 0.22 μm membrane filter. The remaining Pb(II) content was quantified by ICP-OES and ICP-MS.

Drip test: Each damaged cell was placed in a funnel at a tilt angle of approximately 30°. DI water was continuously dripped into the cracked area at a rate of 5 mL/h for 3 hours. The lead concentration in the contaminated water was collected using a centrifuge tube at the bottom of the funnel and then further quantified by ICP-OES and ICP-MS.

Simulated acid rain test: For the simulated acid rain soak and drip tests, a solution with pH=4.2 (adjusted with HCl and NaOH) was used instead of DI water. In the ion competition test, $CaCl_2$ and $MgCl_2$ were added to simulated acid rain at pH=4.2 as above to produce a solution with Ca^{2+} and Mg^{2+} concentrations of 10 mg/L.

The Optical Simulation.

As mentioned in the article, the optical simulation is performed using an open-source modelling platform, EYcalc. The optical module calculates the absorptance of each layer of the given stack, total reflectance and transmittance, combining transfer matrix for thin films and series expansion of Beer-Lambert for thick optically incoherent layers. We carried out the simulations by building up a database of the refractive indices of the materials used in our PSC.

Supplementary note.

Pb(II) sorption kinetics of PFPF: The adsorption kinetics tests were analyzed by pseudo-first-order and pseudo-second-order models. The pseudo-first-order kinetic model can be represented as follows:

$$q_t = q_e(1 - e^{-K_1 t})$$

where q_e is the adsorption capacity (mg/g) of the adsorbent at equilibrium, K_1 (min^{-1}) is the equilibrium rate constant of the pseudo-first-order adsorption. The experimental data plot of the pseudo-first-order kinetic model and which fitting of the kinetic adsorption results are shown in Figure 3g.

The pseudo-second-order kinetic model can be represented as follows:

$$q_t = \frac{tK_2q_e^2}{1 + tKq_e}$$

where K_2 (g min^{-1} mg^{-1}) is the equilibrium rate constant for the pseudo-second-order model. The experimental data plot of the pseudosecond-order kinetic model and which fitting of the kinetic adsorption results are shown in Figure S13.

The Weber-Morris intra-particle kinetic models have been used to derive the rate-limiting step. The Weber–Morris intra-particle kinetic model can be represented as follows:

$$q_t = K_{MW}t^{\frac{1}{2}} + C$$

where K_{MW} (mg g^{-1} $t^{-1/2}$) is the intra-particle diffusion coefficient, and C is the constant that is associated with the thickness of the boundary layer. The experimental data plot of the Weber-Morris intra-particle kinetic models and which fitting of the results are shown in Figure S14.

Pb(II) sorption isotherm test of PFPF: The adsorption isotherm tests were analyzed by Langmuir and Freundlich isothermal adsorption models.

Langmuir isothermal adsorption model can be represented as follows:

$$\frac{C_e}{q_e} = C_e \times \frac{1}{q_{max}} + \frac{1}{K_L q_{max}}$$

Where q_e (mg g^{-1}) is the sorption capacity at equilibrium state, C_e (mg L^{-1}) is the Pb concentration remaining in the solution at equilibrium state and K_L (L mg^{-1}) is a constant related to binding site affinity. The fitting results are shown in Figure 3h.

Freundlich isothermal adsorption model can be represented as follows:

$$q_e = K_F C_e^{-n}$$

Where q_e (mg g^{-1}) is the sorption capacity at equilibrium state, C_e (mg L^{-1}) is the Pb concentration remaining in the solution at equilibrium state and K_F (mg/g) is the Freundlich constant, and n is the adsorption intensity index. The fitting results are shown in Figure S15.

The interfacial Fresnel reflection coefficient: The optical reflection loss at the interface of different media can be expressed by the Fresnel equation:

$$R = \left(\frac{n_1 - n_0}{n_1 + n_0}\right)^2$$

where n_0, n_1 are the corresponding refractive indices of the media beside the interface and R is the interface reflectance.

2. Figures

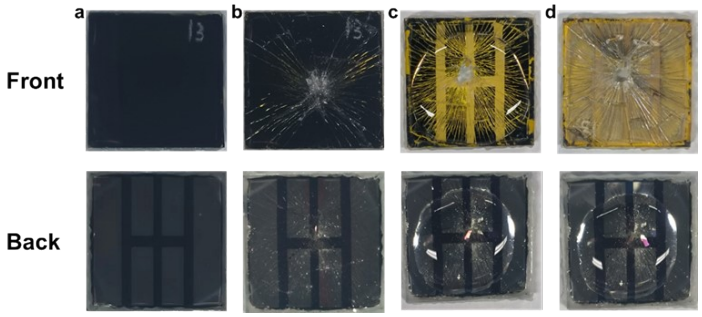

Figure S1. Photographs of encapsulated PSCs after external impacts. Glass (front) and metal (back) side of the encapsulated PSC before (a) and after (b) broken by a metal ball, respectively. Star-shaped microcracks appeared on the front of the PSC while the glass cover on the back remained intact. Photographs taken 1 minute (c) and several hours (d) after dripping deionized water on the front and back of the PSC. The fronts of the PSC turned yellow rapidly after dripping water, indicating that the frontal cracks were sufficiently shattered and that the water was completely immersed into the PSC within 3 h. On the other hand, the absence of visible phenomenon on the back side indicates that the glass cover remains intact after impacts.

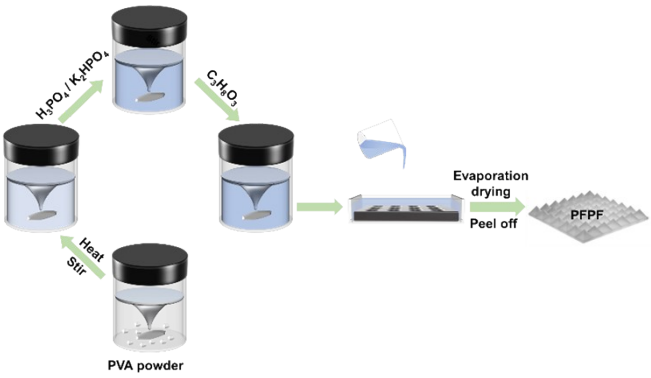

Figure S2. Schematic illustration showing the preparation process of PFPF. The PFPFs were prepared by a simple one-pot reaction with polyvinyl alcohol (PVA), phosphoric acid (H_3PO_4), dipotassium hydrogen phosphate (K_2HPO_4) and glycerol ($C_3H_8O_3$). PVA featuring high optical transmittance, low cost, and dopant-dependent thermal and electrical properties was used as the polymer matrix.[3, 4] Pb^{2+} sequestration agent (i.e., H_3PO_4 and K_2HPO_4), showing pH buffering capability was used to immobilize Pb^{2+}. $C_3H_8O_3$ was used as a plasticizer for PVA because of their hydrogen bonding interaction, which enhanced the flexibility and toughness of the polymer film.[5-7]

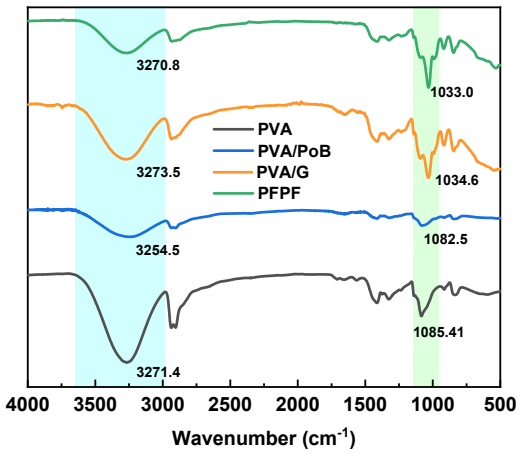

Figure S3. FTIR spectra after adding different additives to PVA. The peaks at 3271.4 and 1085.4 cm^{-1} are attributed to the stretching vibrational peaks of -OH and C-O in PVA. After the addition of H_3PO_4 and K_2HPO_4 (i.e., PVA/PoB), both of these peaks are shifted to lower wavelengths of 3254.5 and 1082.5 cm^{-1}, respectively. This is due to the formation of hydrogen bonding between P-OH and P=O on the phosphate compound and the -OH of PVA. When $C_3H_8O_3$ was added to PVA as a plasticizer (PVA/G), the hydrogen bonds between the molecular chains of PVA are weakened, evidenced by the shift of two characteristic peaks to 3273.5 and 1034.6 cm^{-1}. Therefore, $C_3H_8O_3$ was added to PVA/PoB to improve the mechanical properties. Indeed, the peaks of -OH and C-O of PFPF were blue-shifted to 3270.8 and 1033.0 cm^{-1} compared to PVA.

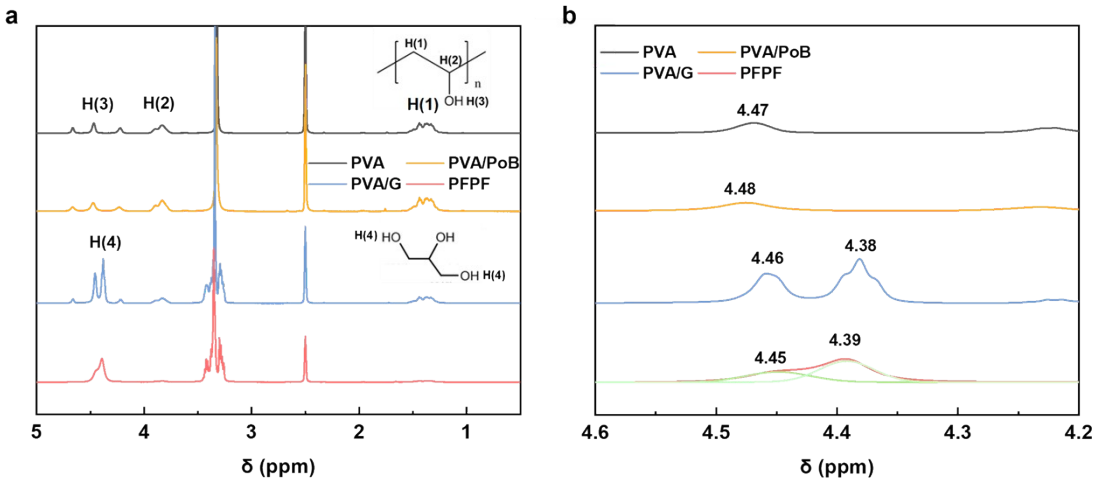

Figure S4. 1H-NMR spectra (a) after adding different additives to PVA in DMSO-*d*6 and (b) partial enlargement of the spectra. The curves have been corrected for the characteristic peaks of the solvents. Hydrogen bonding interactions between the components were demonstrated by shifts in the H(3) and H(4) peaks.

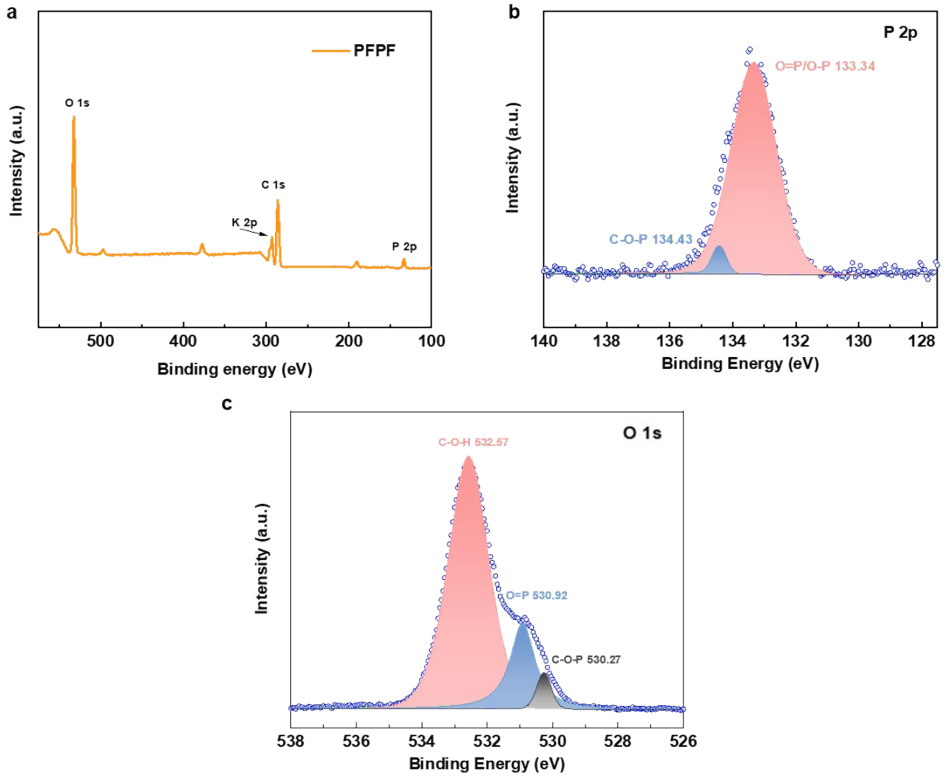

Figure S5. (a) XPS survey spectrum of PFPF. High-resolution XPS spectra of the PFPF for (b) P 2*p* and (c) O 1*s*.

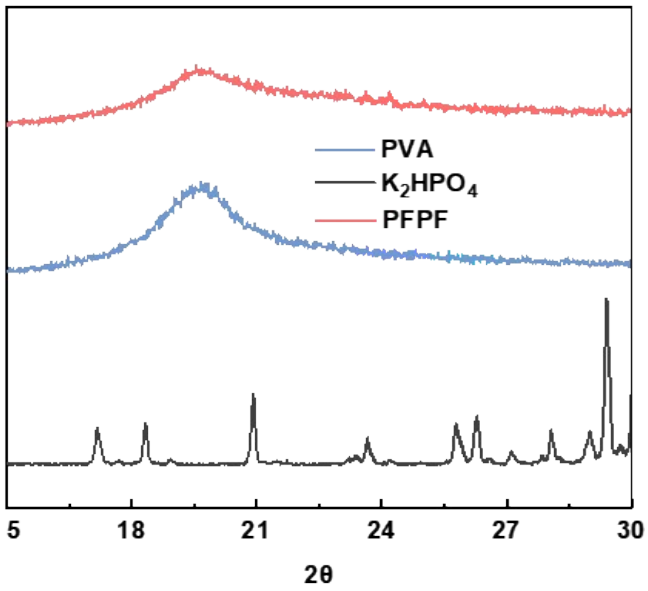

Figure S6. The chemical structure of the phosphate buffer functionalized polymers.

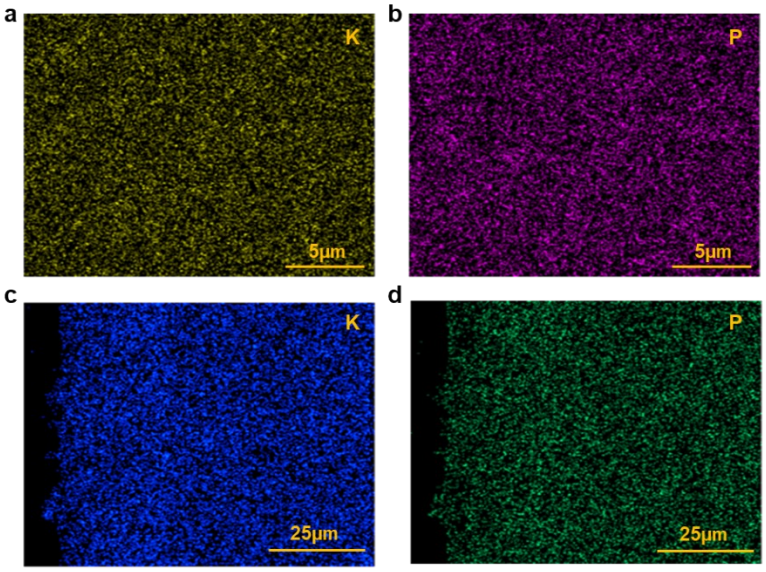

Figure S7. EDS image of PFPF. EDS images of K element distribution in (a) frontal and (c) cross-sectional sections of PFPF. EDS images of P element distribution in (b) frontal and (d) cross-sectional sections of PFPF. K_2HPO_4 is uniformly dispersed in PFPF as shown by the uniform distribution of K and P elements in PFPF.

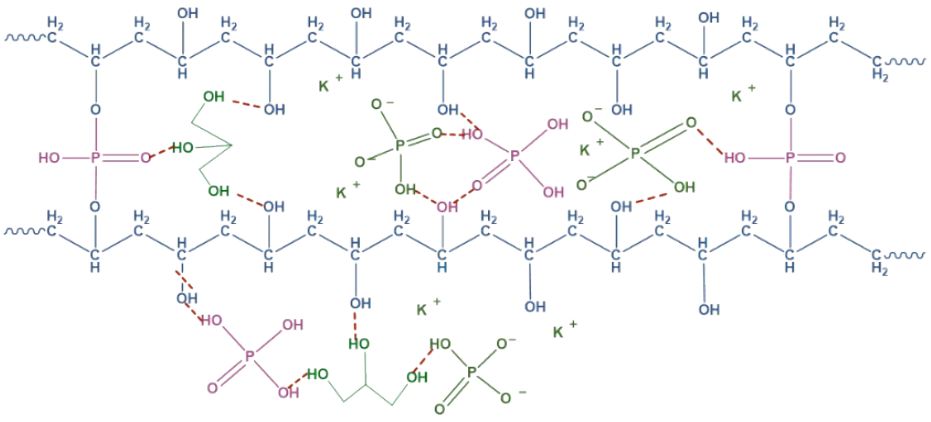

Figure S8. Molecular structure of PFPF.

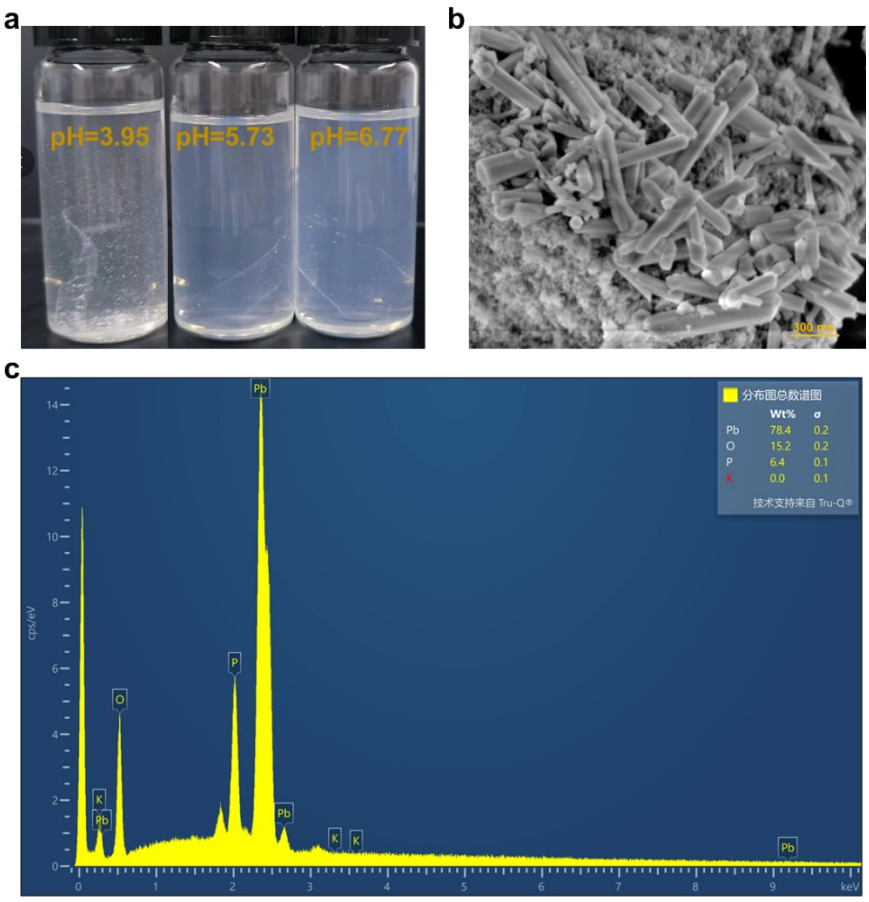

Figure S9. Precipitation morphology and structure. Photographs (a) and SEM image (b) of precipitates produced by the reaction of PFPF with PbI_2 solution. When different formulations of PFPF were added to PbI_2, the solution became turbid at an extremely rapid rate. (c) Ratio of elements in precipitation. The weight ratio of each element in the precipitate demonstrated by the EDS test is essentially the same as the theoretical weight ratio.

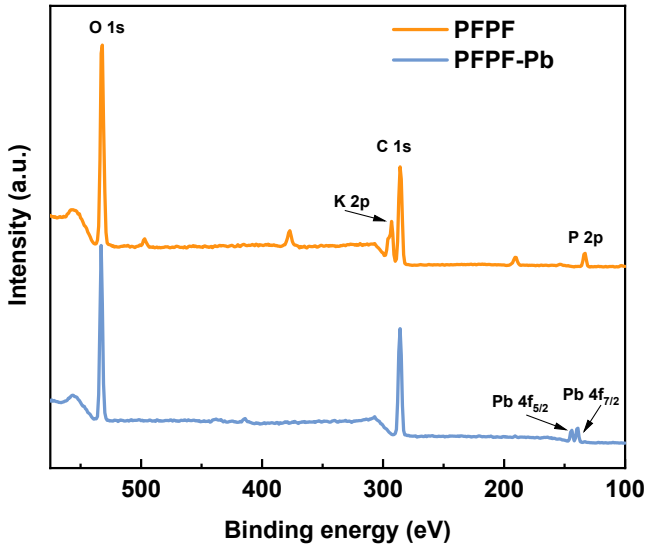

Figure S10. XPS survey spectrum of PFPF and PFPF-Pb.

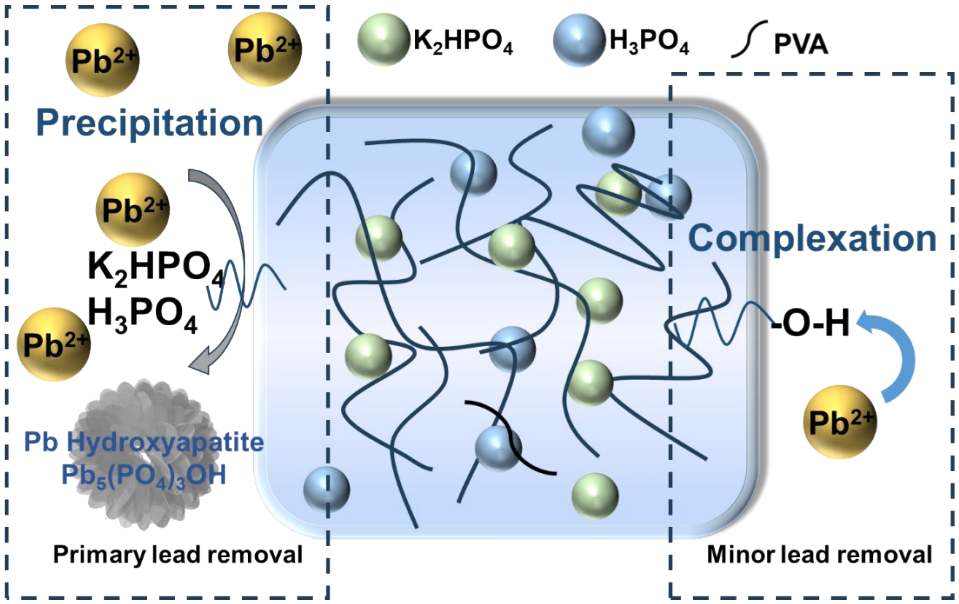

Figure S11. Mechanism of Lead Sequestration of PFPF. PFPF contains multiple hydrogen bonds. A small amount of phosphoric acid is esterified with PVA, but breaks under the catalysis of Pb^{2+}, and then reacts with lead to precipitate. PFPF mainly removes lead and lead by forming precipitation with lead, and a small amount of lead is removed by forming complexation with PVA.

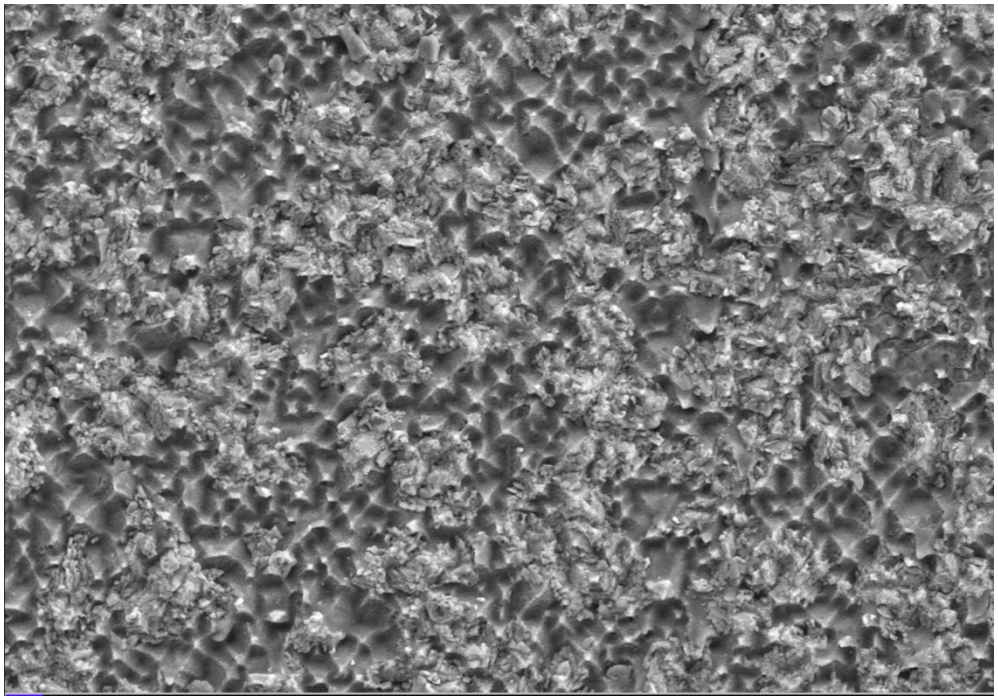

Figure S12. SEM images of K_2HPO_4 when used in excessive amounts in PFPF. White K_2HPO_4 prevents the transmission of light.

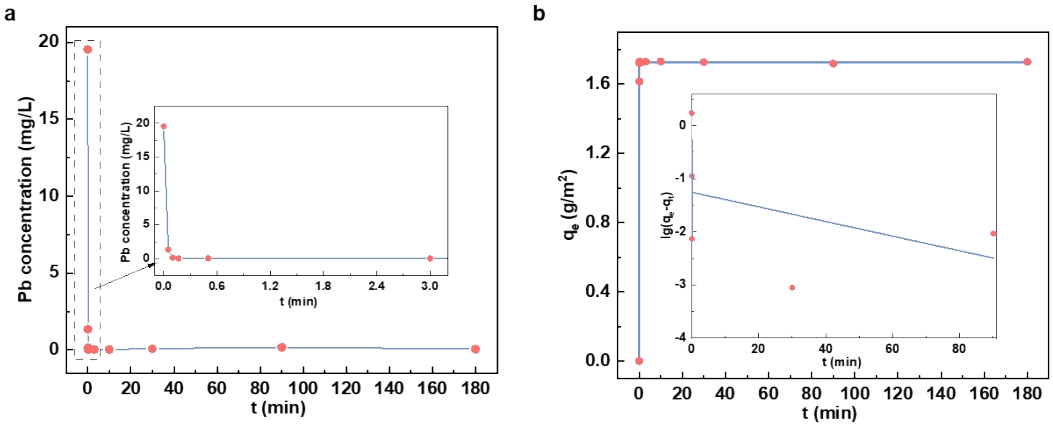

Figure S13. Kinetic experiments on PFPF sequestered lead. (a) The curve of lead concentration in solution after addition of PFPF. (b) The kinetics fitting curve of the PFPF from a pseudo-first-order mode (R^2=0.144).

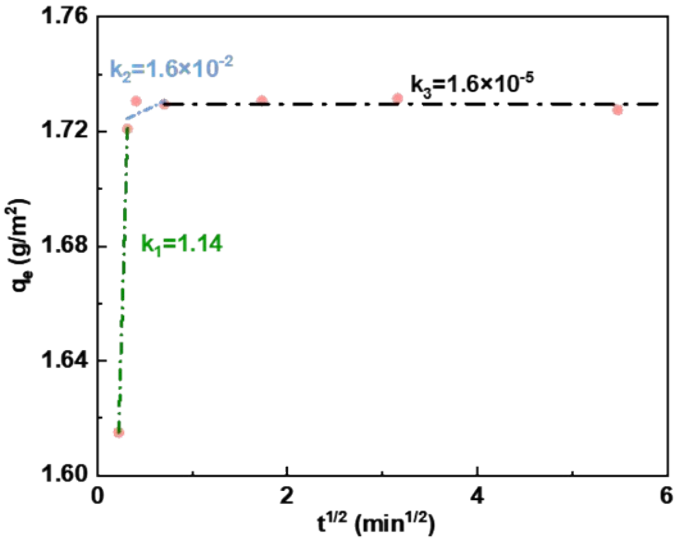

Figure S14. The Pb^{2+} absorption of the PFPF fitted using Weber-Morris kinetic models.

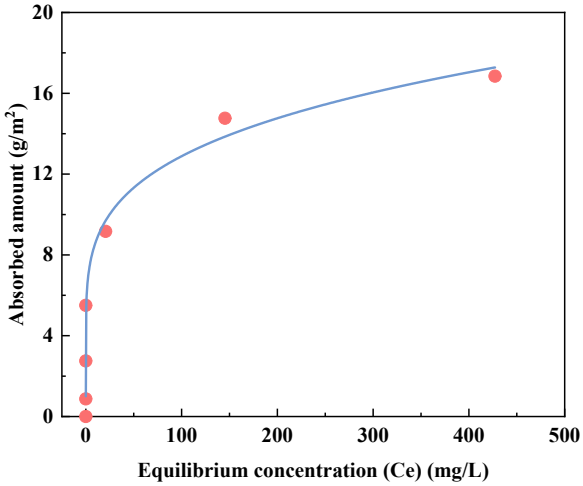

Figure S15. The kinetics fitting curve of the PFPF from a Freundlich isothermal adsorption model (R^2=0.905).

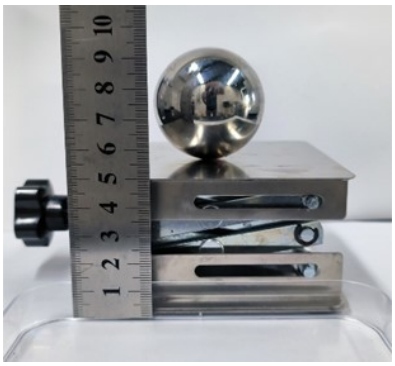

Figure S16. Photograph of the metal ball impact perovskite solar cell to simulate hail impact.

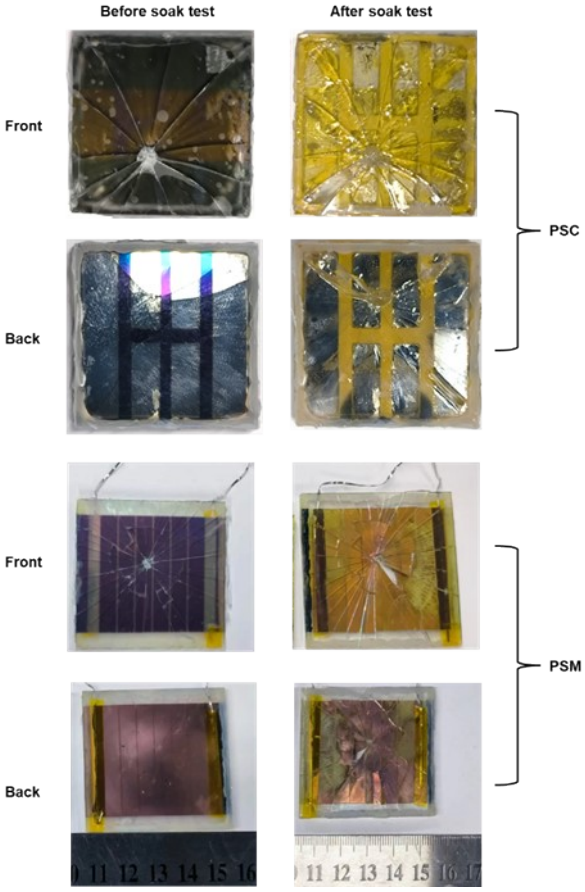

Figure S17. Photographs showing the damaged PSC and PSM before and after water soaking test. After the water soak test, the black perovskite layer changed to yellow or transparent, indicating that the PSC was fully submerged in water and the lead ions had leaked significantly.

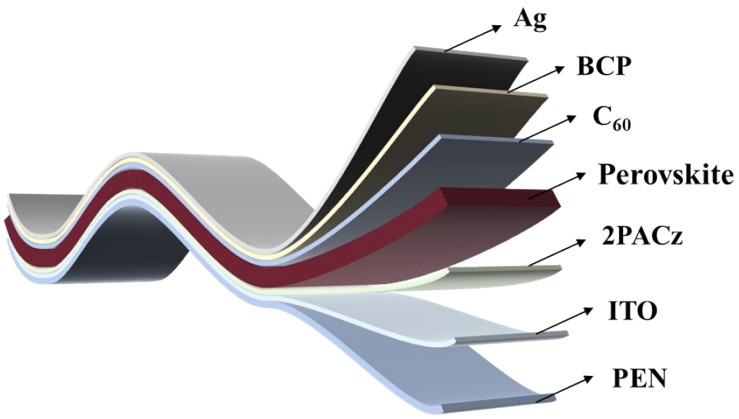

Figure S18. Schematic structure of flexible PSCs.

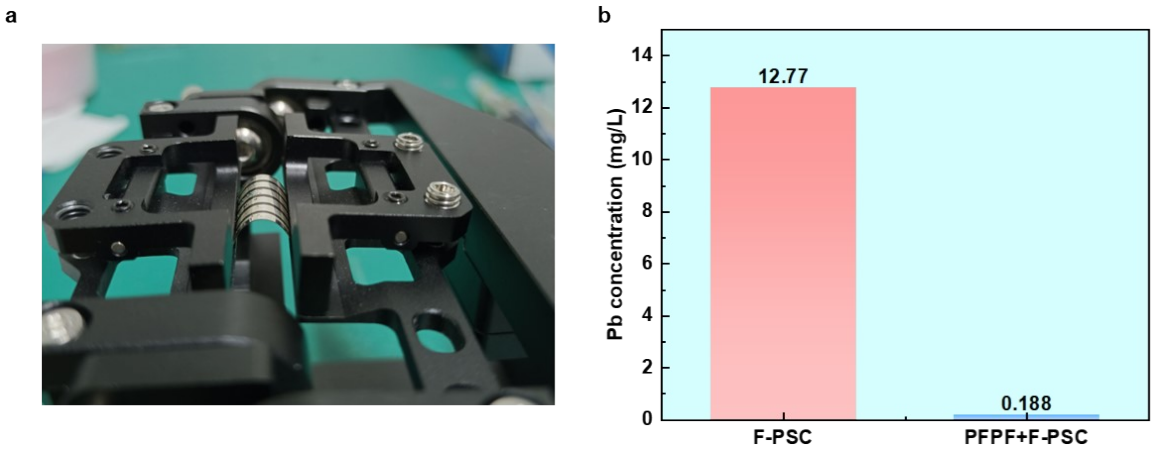

Figure S19. (a) Photographs of bent flexible PSC. (b) Water soaking test results for the damaged encapsulated F-PSC without and with the PFPF after blending.

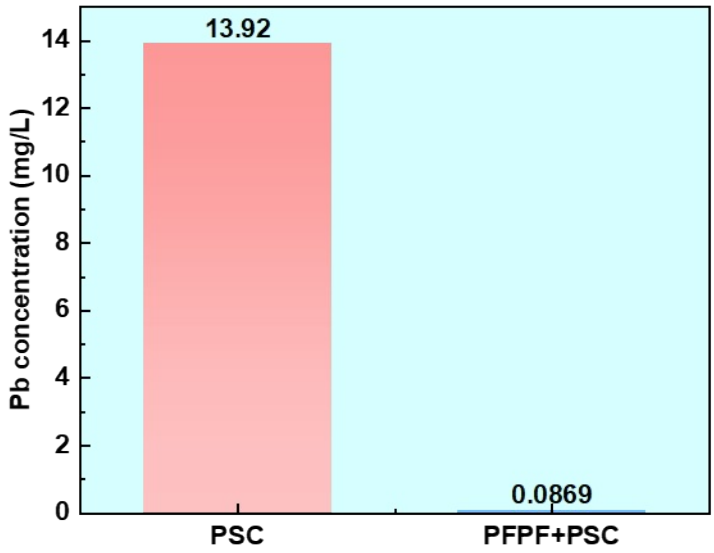

Figure S20. Water soaking test results for the damaged encapsulated PSCs without and with the PFPF at 85℃.

Figure S21. Photographs of acid water with a pH value of 4.2 dripped on the damaged PSCs for 3h with adripping rate of 5 mL h^{-1} to simulate weather condition of acid rain after hail impact on PSCs.

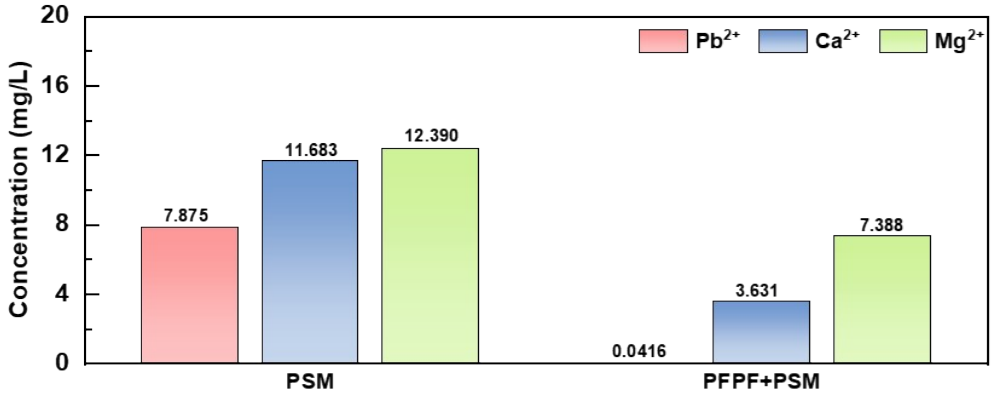

Figure S22. Simulation of the effectiveness of PFPF in preventing lead leakage from PSM in acidic and ionic competition environment.

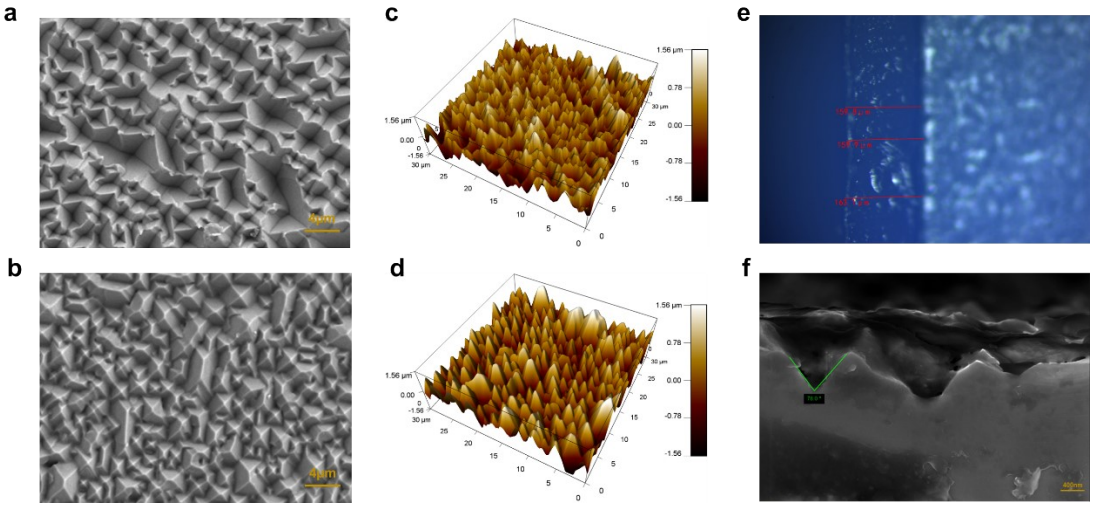

Figure S23. Microscopic image of PFPF. SEM (a, b) and AFM (c, d) images of template wafers and PFPF. The positive pyramidal mechanism of the PFPF surface and its roughness, which is similar to that of the template wafer, indicate the successful replication of the surface morphology of the template wafer. (e) Film thickness of PFPF. (f) The angle of the top corner of the pyramid.

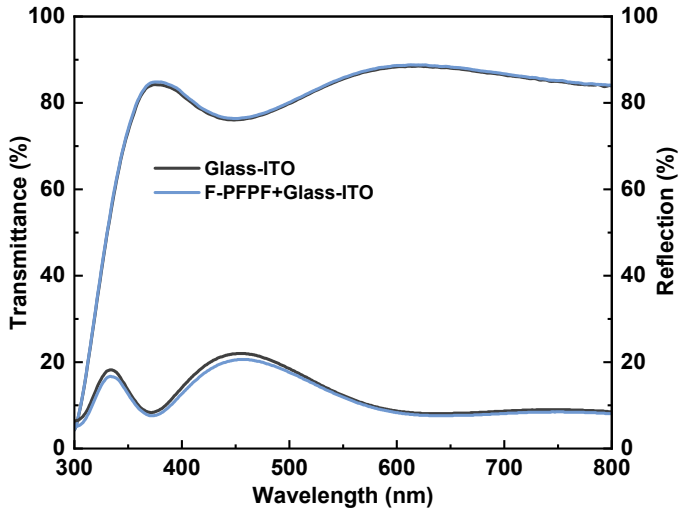

Figure S24. Transmission and reflection of the ITO glass substrate with and without F-PFPF.

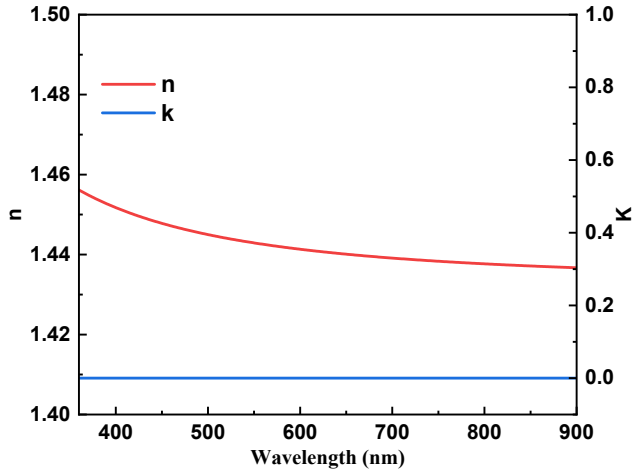

Figure S25. Refractive index (n) and extinction coefficient (k) of the PFPF.

In addition, we further calculated the light transition efficiency (LTE) of devices without and with PFPF. The LTE of theoretical light transmission efficiency is calculated by the Fresnel equation (*Advanced Energy Materials, 2022, 12(33): 2201520*).

$$LTE = \frac{4n_t n_i}{(n_t + n_i)^2}$$

where n_i is the refractive index of the incident material of light, and n_t is the refractive index of the transmitting material of light. As a result, the LTE of PFPF is higher (96.75%) than glass (95.61%) due to the lower refractive index (n_{air}=1, n_{PFPF}=1.44, n_{glass}=1.53). This results in an improvement in PCE of PSCs.

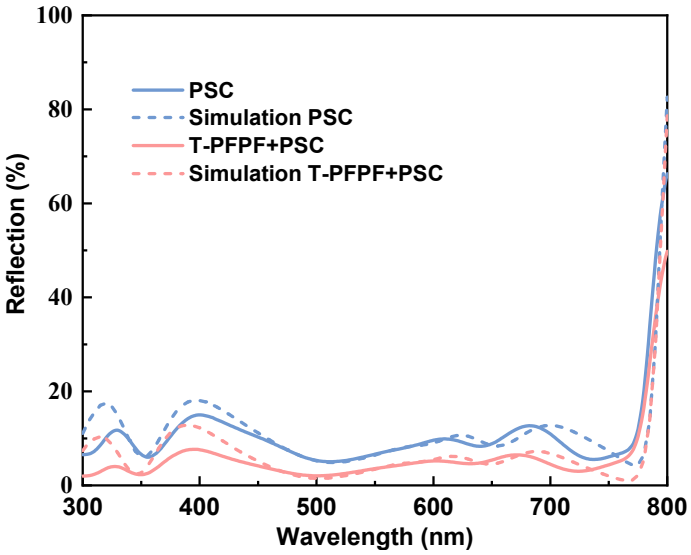

Figure S26. The experiment and emulation reflection of PSC with and without PFPF.

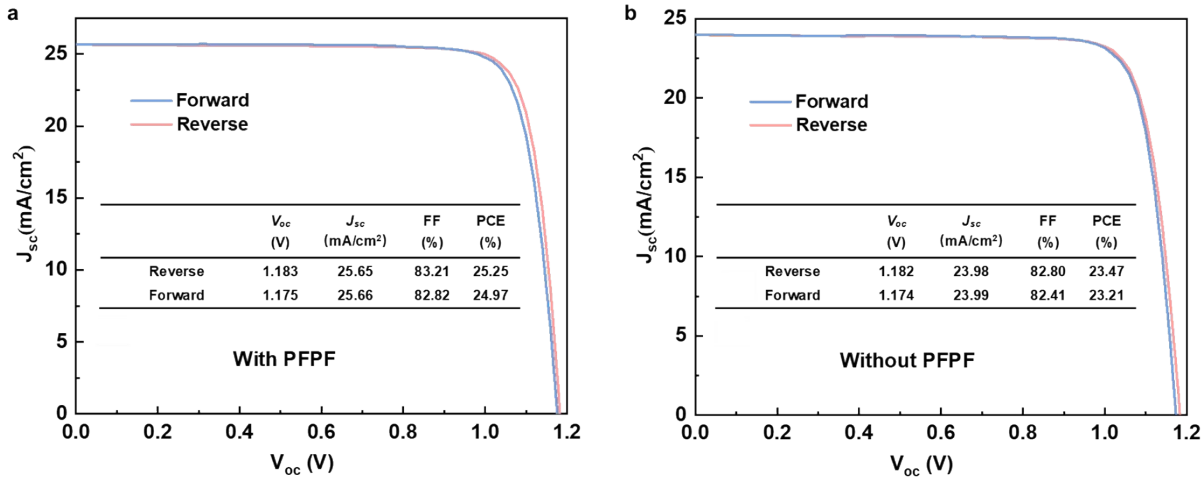

Figure S27. J–V curves and photovoltaic parameters of the champion rigid PSC with and without PFPF under different scan directions.

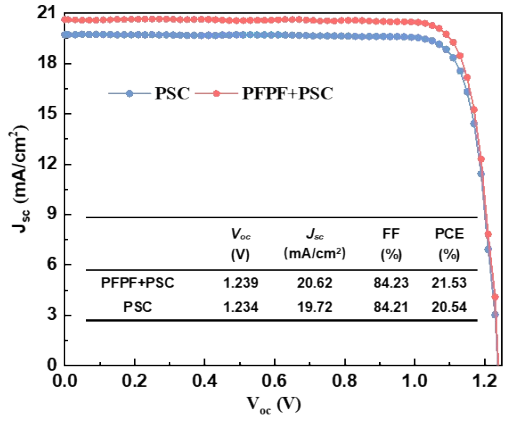

Figure S28. J–V curves and photovoltaic parameters of the wide bandgap PSCs with and without PFPF.

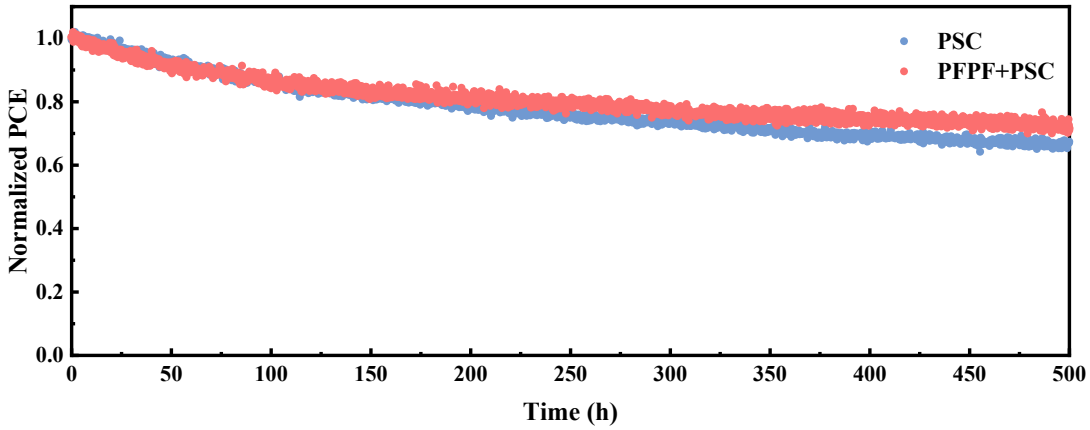

Figure S29. Normalized efficiency of the PSCs without and with the PFPF performed at MPP.

3. Tables

Table S1. The estimated equilibrium time and the maximum adsorbing capacity of the reported Pb-absorbing materials and the PFPF.

Pb^{2+} sequestration materials	estimated equilibrium time (min)	maximum adsorbing capacity (g m^{-2})	Reference
CNT-PAA	5	NA	8
POM@MOF	5	NA	9
POMOF	5	NA	10
CER	20	NA	11
CER	20	NA	12
Ionogel	20	27.14g/m^2	13
S-GA	30	NA	14
DMDP	30	1.28 g/m^2	15
ZrL_3:bis-C_{60}	30	NA	16
PPVI-TFSI	30	NA	17
HDA-HBPs	30	NA	18
CPD	260	0.828 g/m^2	19
HOF-FJU-1	400	NA	20
TiO_2 sponge	480	0.63 g/m^2	1
PFPF	**0.167**	**17.205 g/m^2**	

Table S2. Statistical photovoltaic parameters of PSCs with and without PFPF.

	V_{oc} (V)	J_{sc} (mA/cm^2)	FF (%)	PCE (%)
PFPF+PSC	1.172±0.007	25.58±0.12	81.30±1.45	24.38±0.56
PSC	1.171±0.006	24.02±0.31	80.97±1.06	22.77±0.48
PFPF+F-PSC	1.112±0.003	24.26±0.09	82.24±0.36	22.20±0.04
F-PSC	1.110±0.004	22.71±0.07	81.48±0.48	20.54±0.14

A total of 10 samples (5 PSCs with PFPF and 5 PSCs without PFPF) were considered for statistical analysis.

Table S3. Comparison of the other Pb-absorbing materials.

Materials used in previous reports	Materials cost ($/g)	Reference
Self-healing resin	342	[2]
DMDP	16500	[15]
EDTMP	0.625	
CERs	0.24	[11]
S-GA/PDMS	0.133	[14]
CPD	0.048	[19]
PFPF	**0.019 (This work)**	

4. References

1. S. Valastro, E. Smecca, G. Mannino, C. Bongiorno, G. Fisicaro, S. Goedecker, V. Arena, C. Spampinato, I. Deretzis, S. Dattilo, A. Scamporrino, S. Carroccio, E. Fazio, F. Neri, F. Bisconti, A. Rizzo, C. Spinella, A. La Magna and A. Alberti, *Nat. Sustain*, 2023, **6**, 974-983.
2. Y. Jiang, L. Qiu, E. J. Juarez-Perez, L. K. Ono, Z. Hu, Z. Liu, Z. Wu, L. Meng, Q. Wang and Y. Qi, *Nat. Energy*, 2019, **4**, 585-593.
3. C. U. Devi, A. K. Sharma and V. V. R. N. Rao, *Mater. Lett.*, 2002, **56**, 167-174.
4. H. E. Ali, I. Morad, H. Algarni, M. M. El-Desoky, Y. Khairy, H. Y. Zahran and I. S. Yahia, *J. Mater. Sci.: Mater. Electron.*, 2021, **32**, 4466-4479.
5. O. Hu, G. Chen, J. Gu, J. Lu, J. Zhang, X. Zhang, L. Hou and X. Jiang, *Int. J. Biol. Macromol.*, 2020, **164**, 2512-2523.
6. C. Hu, Y. Zhang, X. Wang, L. Xing, L. Shi and R. Ran, *ACS Appl. Mater. Interfaces*, 2018, **10**, 44000-44010.
7. H. Chen, X. Ren and G. Gao, *ACS Appl. Mater. Interfaces*, 2019, **11**, 28336-28344.
8. J. Wang, R. Zhang, H. Xu, Y. Chen, H. Zhang and N.-G. Park, *ACS Energy Lett.*, 2022, **7**, 1577-1585.
9. Y. Dong, J. Zhang, Y. Yang, J. Wang, B. Hu, W. Wang, W. Cao, S. Gai, D. Xia, K. Lin and R. Fan, *Nano Energy*, 2022, **97**, 107184.
10. Y. Dong, J. Zhang, W. Wang, B. Hu, D. Xia, K. Lin, L. Geng and Y. Yang, *Small*, 2023, **19**, 2301824.
11. Z. Li, X. Wu, S. Wu, D. Gao, H. Dong, F. Huang, X. Hu, A. K. Y. Jen and Z. Zhu, *Nano Energy*, 2022, **93**, 106853.
12. S. Chen, Y. Deng, H. Gu, S. Xu, S. Wang, Z. Yu, V. Blum and J. Huang, *Nat. Energy*, 2020, **5**, 1003-1011.
13. X. Xiao, M. Wang, S. Chen, Y. Zhang, H. Gu, Y. Deng, G. Yang, C. Fei, B. Chen and Y. Lin, *Sci. Adv.*, 2021, **7**, eabi8249.
14. Z. Li, X. Wu, B. Li, S. Zhang, D. Gao, Y. Liu, X. Li, N. Zhang, X. Hu, C. Zhi, A. K. Y. Jen and Z. Zhu, *Adv. Energy Mater.*, 2022, **12**, 2103236.
15. X. Li, F. Zhang, H. He, J. J. Berry, K. Zhu and T. Xu, *Nature*, 2020, **578**, 555-558.
16. S. Wu, Z. Li, M.-Q. Li, Y. Diao, F. Lin, T. Liu, J. Zhang, P. Tieu, W. Gao, F. Qi, X. Pan, Z. Xu, Z. Zhu and A. K. Y. Jen, *Nat. Nanotechnol.*, 2020, **15**, 934-940.

17. H. Chen, G.-H. Zhang, Q.-H. Zhu, J. Fu, S. Qin, L. He and G.-H. Tao, *ACS Appl. Mater. Interfaces*, 2023, **15**, 13637-13643.
18. Z. Li, C. Jia, Z. Wan, J. Xue, J. Cao, M. Zhang, C. Li, J. Shen, C. Zhang and Z. Li, *Nat. Commun.*, 2023, **14**, 6451.
19. Y. Xiong, H. Cai, W. Yue, W. Shen, X. Zhu, J. Zhao, F. Huang, Y.-B. Cheng and J. Zhong, *J. Energy Chem.*, 2023, **84**, 311-320.
20. J. Zhang, C. Li, M. Zhu, J. Qiu, Y. Yang, L. Li, S. Tang, Z. Li, Z. Mao, Z. Cheng, S. Xiang, X. Zhang and Z. Zhang, *Nano Energy*, 2023, **108**, 108217.